

The Boundary of X-Ray and Electron Tomography

Zachary H. Levine

National Institute of Standards and Technology, Gaithersburg, MD 20899-8410

(Dated: January 21, 2005)

Samples a few micrometers in total size offer a challenge to both x-ray and electron tomography. X-ray tomography originated imaging the human body with millimeter resolution, but the resolution has been reduced by over 7 orders of magnitude by the use of synchrotron sources and Fresnel zone plates, leading to an achieved resolution of 20 nm in favorable cases. Further progress may require phase retrieval. Electron tomography originated on very thin samples (perhaps 100 nm thick) but recently samples of over 1 micrometer have been studied with conventional instruments. The study of thicker samples requires understanding tomography in the multiple scattering regime.

I. X-RAY TOMOGRAPHY

Although Radon's initial work of 1917 is credited with the foundation of tomography as a mathematical subject, in practice the paper had little immediate impact and was rediscovered during the 1960's during the development of computerized axial tomography, popularly known as CAT scans. This work most notably led to the 1979 Nobel Prize in Physiology and Medicine by Cormack and Hounsfield¹ and is the first of many examples of medical imaging systems in wide use today, including ultrasound and magnetic resonance imaging. The word "axial" has been dropped from more recent x-ray imaging systems leading to "CT scanners" (for computerized tomography) because the data is not acquired about a single axis, but may involve more complex patterns such as fan beams or helical scans.

In its simplest form, tomography is the practice of forming images in two or three dimensions from projections. Projections are defined to be line integrals of some scalar quantity, such as the x-ray absorption coefficient $\alpha(\vec{r})$ which is allowed to vary with the sample position \vec{r} .¹ In the case of axial tomography, the sample is turned about an axis (here taken to be in the \hat{y} direction) and a beam of intensity I_0 penetrates the sample at every small interval (i.e., pixel) of the sample. The intensity I is detected at each offset τ in the sample for many tilt angles θ . To the extent that x-rays obey geometric optics (a very good assumption for medical imaging), the intensity is given by the Beer's law relation

$$I(\tau, \theta) = I_0 \exp \left[- \int ds \alpha(\vec{r} + s\hat{\eta}) \right] \quad (1)$$

where the integral is over a path through the sample with an offset vector \vec{r} in the beam direction $\hat{\eta}$. The tilt angle θ relates these co-ordinates to the sample-fixed axes \hat{x} and \hat{z} axes by the rotation

$$\begin{pmatrix} \hat{\eta} \\ \hat{\tau} \end{pmatrix} = \begin{pmatrix} \cos \theta & \sin \theta \\ -\sin \theta & \cos \theta \end{pmatrix} \begin{pmatrix} \hat{x} \\ \hat{z} \end{pmatrix}.$$

With the tilt axis at right angles to the sample, a two-dimensional formalism suffices to solve the problem. The most commonly used method is known as "filtered backprojection", which relies on the Projection Slice Theorem to related one-dimensional Fourier coefficients of the measured projections to two-dimensional Fourier coefficients of the full sample.¹⁻³ Three-dimensional images are obtained simply by repeating the two-dimensional inversion in the third dimension.

Although the resolution in medical tomography has slowly improved through the years, it remains scaled to a millimeter, principally because of radiation risk to the patients. However, in 1983, Grodzins⁴ observed that tomography could be applied to much smaller samples using synchrotron radiation. By 1987, this had been implemented at 15 μm resolution in a study of the porosity of rocks for application in the oil industry.^{5,6} The initial implementation used the technology described in the paragraph above. By 1992, the resolution was improved to 3 μm .^{7,8}

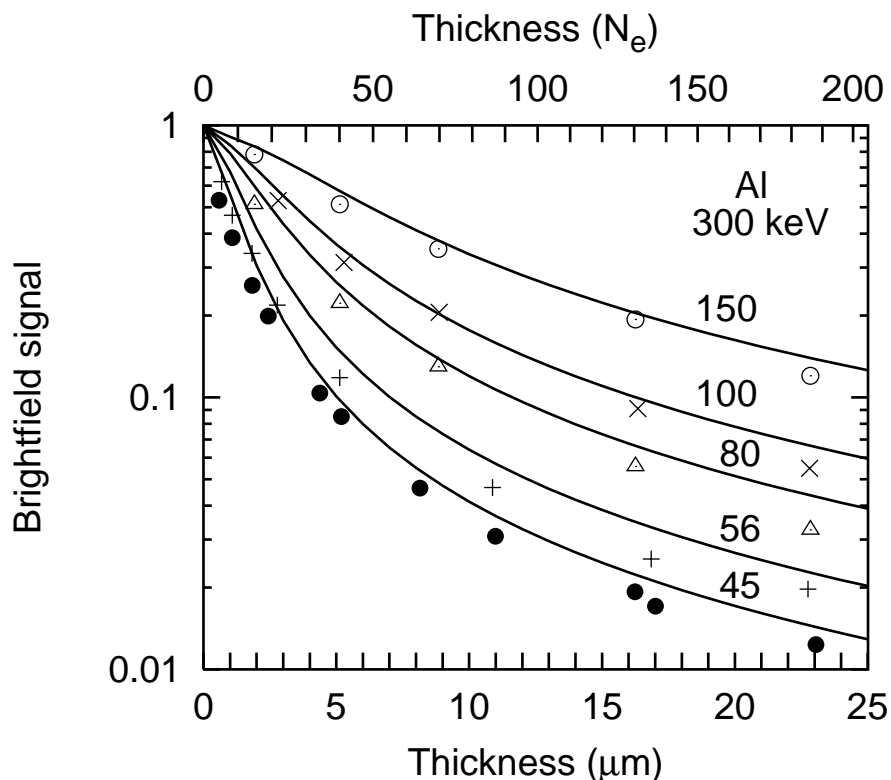


FIG. 1: Transmission of electrons at 300 keV through various thicknesses of aluminum foil into detectors with half-angles marked in mrad. The experimental data of Soum *et al.*⁹ are compared to the summation of the Goudsmit-Saunderson series using the elastic scattering cross sections of Berger and Seltzer¹⁰ and the parameters $\tau = 129$ nm and $\tau^{(1)} = 224$ μm which are derived from the data base of Berger and Seltzer¹⁰ and the aluminum bulk density. There are no free parameters in the fit. The thickness is given both in terms of μm and the number of elastic scattering events N_e .

The introduction of x-ray optics into an x-ray microscopy beamline allowed the dramatic improvement of resolution to 50 nm in 1994.¹³ Specifically, the group used a Fresnel zone plate in a Scanning Transmission X-ray Microscope (STXM) to scan a test object consisting of metal bars on a silicon nitride membrane.¹⁴ Interest continued in this line with application to biology¹⁵ and to integrated circuit interconnects.^{16,17} For biology, there is at least one dedicated beamline operating a full-field microscope today.¹⁸ A resolution of 60 nm for a full yeast cell has recently been reported.¹⁹ Similarly, tomography of integrated circuit interconnects has moved to commercial application.²⁰

The resolution of the microscopes is limited by ability to construct the Fresnel zone plates.^{21,22} Most state-of-the-art zone plates are constructed with electron beam writing with resolution as little as 20 nm.²³ Very recently, a zone plate was constructed using the interference pattern of two zone plates exposed with extreme ultraviolet light to make a zone plate with features half as large — 60 nm in the scientific literature²⁴ but just 13 nm resolution in a more recent news account.²⁵ It is a challenge to make high precision zone plates because of the stability required for the electron beam writing, because of the circular pattern (in a world tuned to writing lines), and because of the high aspect ratio of the zones which can be on the order of 20 in the case of hard x-ray zone plates (for use above, say, 5 keV).

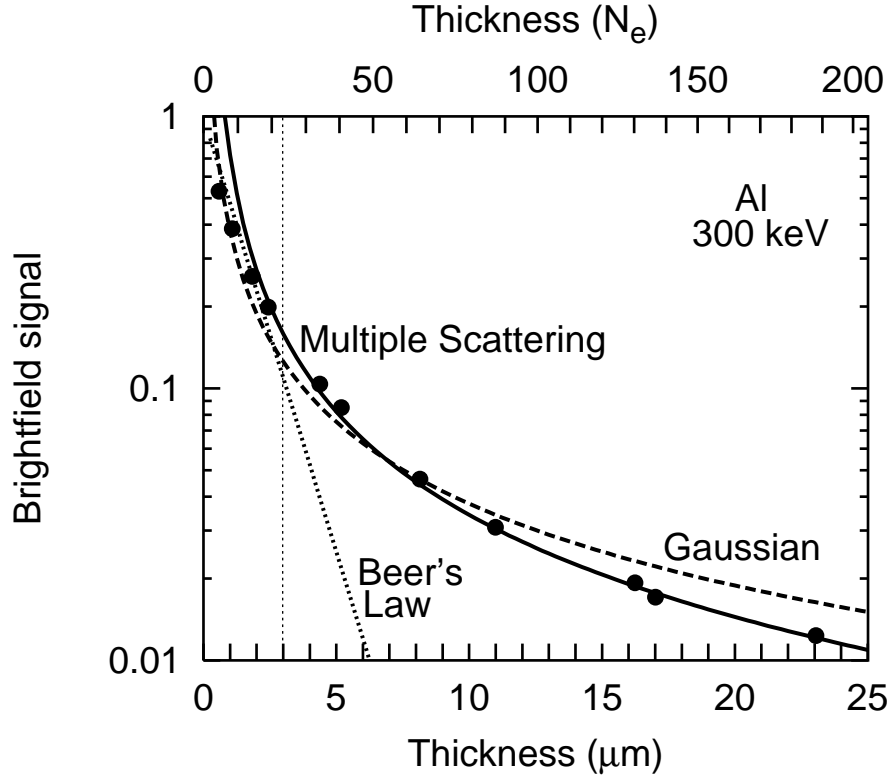


FIG. 2: Transmission of electrons at 300 keV through various thicknesses of aluminum foil into a 45 mrad half-angle on-axis detector, with single parameter fits to the multiple scattering prediction $((t/\tau') \ln(t/\tau'))^{-1}$, the Gaussian model $1/t$, and Beer's Law. The data of Soum *et al.*⁹ are shown. The vertical dotted line is the lower limit of validity of the multiple scattering approximation given by Molière.¹¹

A. Phase retrieval

Phase retrieval may provide an alternative means of obtaining high resolution with x-ray tomography. A resolution of 60 nm has been obtained in a recent experiment,^{26,27} although this in no sense exhausts the power of the technique. Crystal diffraction is sensitive to atomic positions, and, in principle, phase retrieval may achieve comparable accuracy limited by the wavelength of the x-rays.

In phase retrieval, information about the modulus of the intensity transmitted through the object is obtained in both the real and Fourier domains and an iterative algorithm is used to obtain the complex value of (say) the index of refraction through the field.²⁸⁻³⁰ The role of oversampling (compared to crystal diffraction) has been emphasized.³¹ The terminology means that to satisfy the Nyquist sampling theorem, it proves necessary to measure the diffraction pattern at twice the density which is provided by a Bragg pattern of a crystal. A non-periodic object diffracts with non-zero intensity and permits complete sampling in the sense of Nyquist. On the other hand, the atomicity of a crystal allows the imposition of a different set of constraints which has been exploited for decades. Another approach to phase retrieval is provided by the transport-of-intensity equation.³² The transport-of-intensity equation and Gerchberg-Saxton-type phase retrieval have been combined recently to address the problem of stagnation with the Gerchberg-Saxton approach,³³ Elser has addressed stagnation separately.³⁰

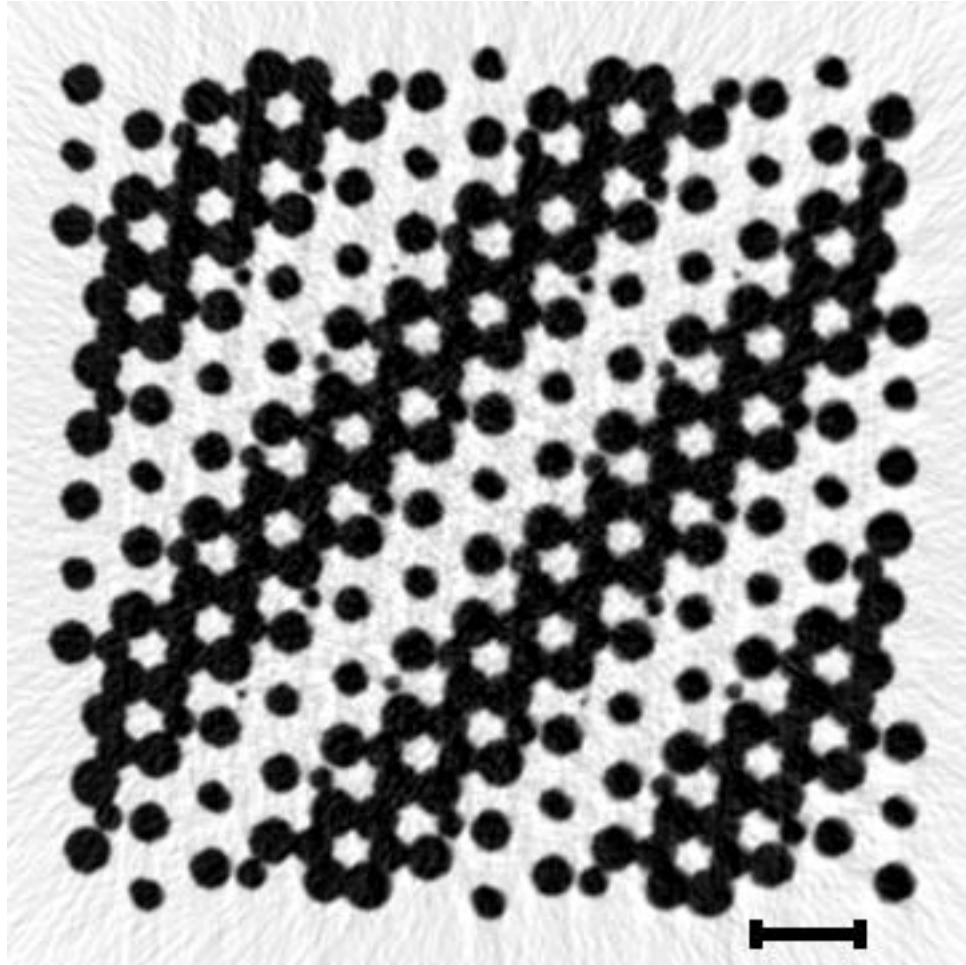


FIG. 3: Reconstructed reverse gray scale image of a simulated photonic band gap crystal using multiple scattering theory. A detector half-angle of 10 mrad is assumed. The saturation values are taken to be the values at the 5th and 95th percentiles of the pixels in the image. The scale bar is 1 μm , which is about the size of the largest tomographic reconstructions based on electron microscopy in the literature.

II. ELECTRON TOMOGRAPHY

Shortly after the introduction of tomography using x-rays, electron microscopes were used for tomography as well on a much shorter length scale.^{34,35} The principal applications have been in microbiology.^{36,37} The practical computational aspects of electron tomography have also been presented.³⁸ Recently, microtubules in a cell have been visualized with a resolution of 8 nm using energy-filtered transmission electron microscopy.³⁹ Electron tomography has also been applied to the case of a tungsten via in an integrated circuit interconnects.⁴⁰

The principal advances have been the use of cryo-freezing to preserve the cell's ultrastructure and the use of minimal dosage (below 1000 electrons per nm^2 for 1 nm resolution).³⁶ The implications of low dosage is partially ameliorated by the existence of the dose fractionalization theorem, which indicates that the dosage required for reconstructing an image with a full tilt series is formally the same as that required to observe a single image.^{41,42}

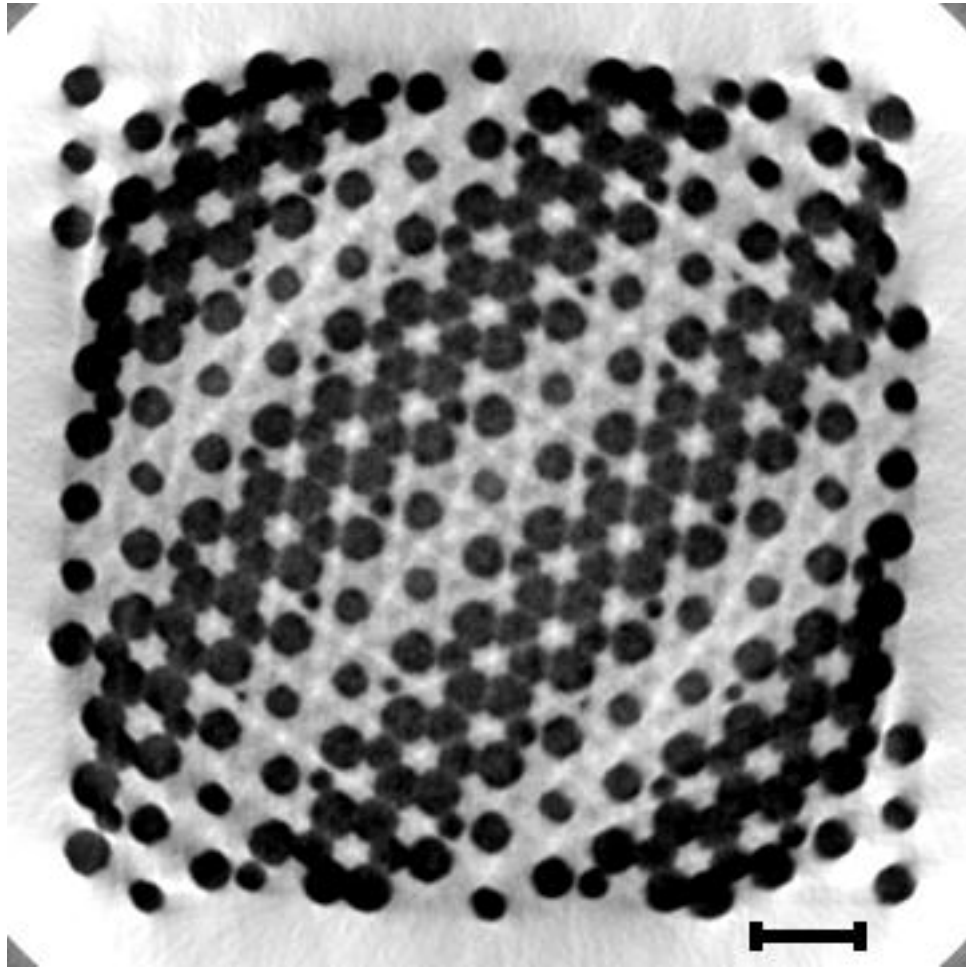


FIG. 4: Reconstructed reverse gray scale image analogous to Fig. 3 but using Beer's Law. The reconstruction is good despite the use of Beer's Law outside its range of validity.

Alignment of images is a great issue for electron tomography. Indeed, with single-particle reconstruction, a great many images of copies of the sample are acquired and these are oriented based on key properties of the individual copies.⁴³ This technique was applied successfully to obtain the structure of the ribosome.⁴⁴ For larger biological samples, typically gold fiducial markers are used to aid in the alignment,⁴⁵ although marker-free methods have also been used.⁴⁶ Because biological samples distort during the acquisition of a tilt series, the fiducials are not used merely as needed to align a rigid body in space, but also to track and undo the effects of distortion.⁴⁵

Although the issues of sample preparation, alignment, and visualization have shown remarkable progress, at the core the Beer's Law relation Eq. (1) between sample thickness and intensity is universally applied in electron microscopy. Yet, in contrast to the x-ray case, the underlying interaction of an electron with a sample is one of multiple scattering.^{47,48} Multiple scattering leads to non-exponential relations between the detected intensity and the sample thickness. Recently, experiments have shown that it is possible to obtain three-dimensional information from scanning transmission electron microscopy (STEM) from samples well in excess of $1\ \mu\text{m}$ thick using advanced⁴⁹ and standard⁵⁰ electron microscopes. It is necessary to use STEM rather than conventional transmission electron microscopy (CTEM) because in the latter case, post-specimen electron lenses image the beam. These lenses are subject to chromatic aberration. For a thick

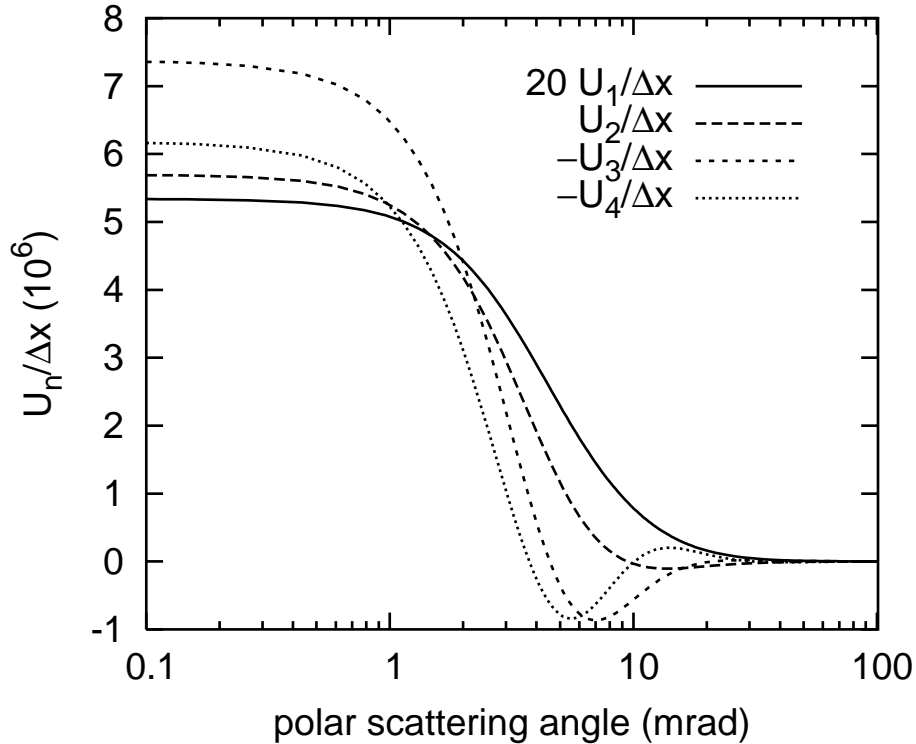


FIG. 5: First angular singular vectors U as a function of angle, normalized to the increments Δx in the cosine of the polar scattering angle in the angular mesh of Berger and Seltzer.¹⁰ The first singular vector represents an average normalized differential cross section for all the elements. The second vector permits accumulation of differential cross section near the forward direction at the expense of large angle differential cross section (or, with opposite sign, the reverse). The third vector enhances the differential cross section near the node of the second vector at the expense of both small and large angle differential cross section. The fourth and higher vectors represent more oscillatory redistributions of differential cross section. Because the elements share a common functional form at large scattering angles, the first singular vector has more weight at large angles than the other singular vectors.

sample, such aberrations may represent the limiting factor on the image resolution because the inelastic losses of the fast electron passing through the sample occur are variable; for example, the plasmon generation is governed by a Poisson distribution and deep, inelastic events only add to the variance.⁵¹ Because the majority of microscopes are conventional, and because there has always been a great desire within the microscopy community to achieve high resolution, the issue of thick samples has languished.

A. Multiple Scattering

The theory of multiple scattering theory for application to tomography has been presented recently.⁴⁸ Here, we limit the discussion to a few key results. Combining the multiple-scattering formalism of Gouldsmit and Saunderson⁵² with the recent compilation of theoretical atomic cross sections,¹⁰ it is possible to obtain parameter-free agreement with experimental data on multiple scattering.⁹ An example is given in Fig. 1.

We may consider three models for the relation of thickness and attenuation for a small bright-field detector: (a) Beer's Law, (b) a Gaussian model, and (c) analytic results from multiple scattering theory. The Gaussian model arises from considering the addition of variance of small angular deviations from a series of thin layers.^{53,54} However, because of the effect of the Rutherford tail, the variance is not well-defined in the small angle approximation and a logarithmic correction to the Gaussian behavior emerges. Whereas the gaussian

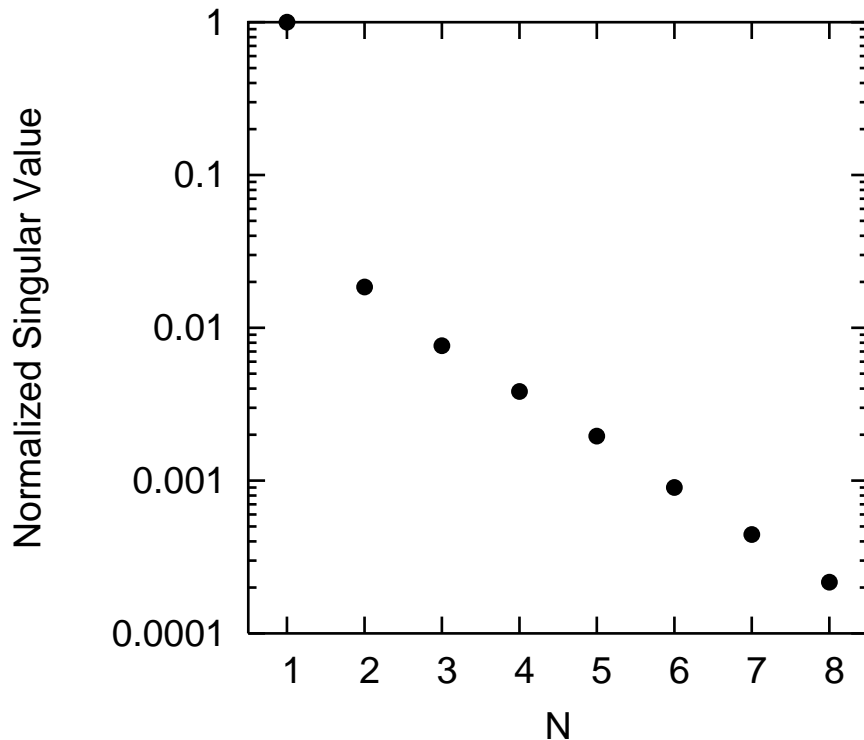


FIG. 6: Singular values of vector space spanned by the normalized elastic cross sections of the first 92 chemical elements minus a δ function. In the first approximation a single component dominates the bright-field signal, however, if the signal to noise ratio exceeds 50, the higher singular values may play a role in the interpretation of the bright-field signal.

predicts an intensity which varies as t^{-1} , multiple scattering theory predicts a dependence of the form $[t \ln(t/\tau')]^{-1}$, where $\tau' = e^{2\gamma-1}\tau$ where γ is Euler's constant and τ is the mean free path. The three models are compared to experimental data in Fig. 2 and the results are fully satisfactory for multiple scattering theory.

The importance of the non-Beer's law relation between the intensity and the thickness is shown in the comparison of Fig. 3 and Fig. 4.⁴⁷ Shown is a reconstruction of Monte Carlo data for a photonic band gap material — a system of polymer and void. The multiple scattering theory leads to a more faithful reproduction of the original sample. In contrast, the Beer's Law model leads to streak artifacts, “photo album corners”, and a “fish-eye lens” effect. Beer's Law does, however, preserve the finer features, as does the multiple scattering reconstruction. One important feature of the simulation of Fig. 3 and Fig. 4 is the scale: the sample is a square 8 μm on a side, whereas nearly all electron tomography is performed with samples no more than 1 μm across.

When the sample consists of a heterogeneous mixture of materials, what exactly do the intensities recorded in an electron microscope correspond to? In the case of x-rays governed by a material-dependent absorption coefficient, one simply integrates as in Eq. (1). In the electron case, the situation is more complicated: there is no single parameter which may be called the “scattering power”. Instead, we must consider the scattering cross sections. In a second paper, Goudsmit and Saunderson extended their theory to include the multiple-component case.⁵⁵ In the approach of Ref. 48, the cross sections of the first 92 elements are taken to span a vector space. Because all the cross sections are similar, there is a “common mode” cross section, which is shown in Fig. 5 along with corrections to that mode which are a series of orthogonal functions. The dominance of the common mode is seen in Fig. 6 to be substantial, but not necessarily rendering the others

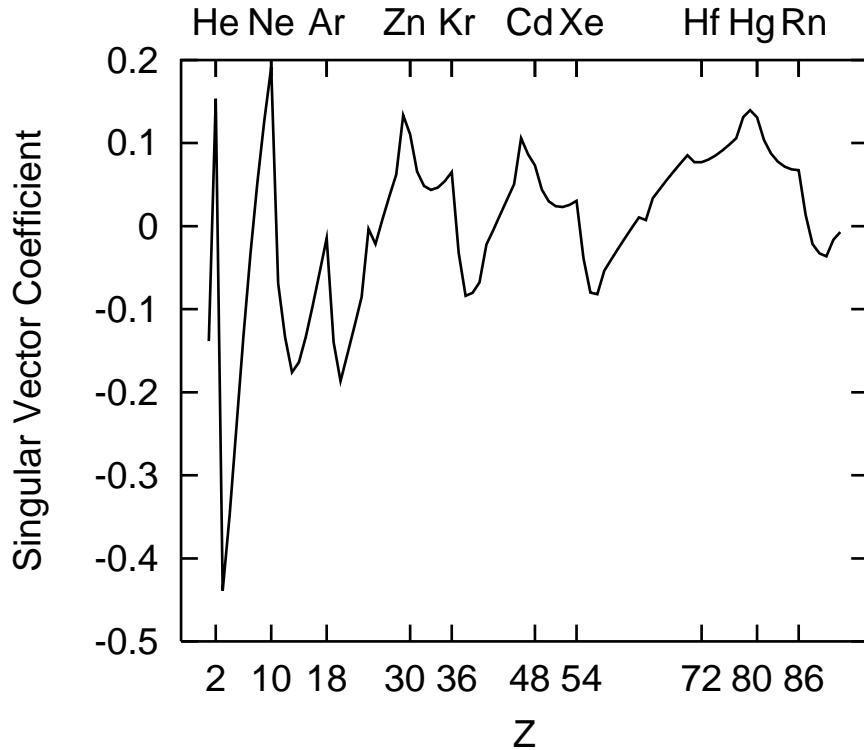


FIG. 7: The coefficients of the second singular vector which are indexed by the atomic number Z from 1 to 92. The coefficients' values are strongly affected by the closing of atomic shells (indicated by the tick marks).

— and particular the second singular vector — unobservable. The various elements may be distinguished as indicated in Fig. 7. Thus, this first singular vector is sensitive to whether the element is located on the left or the right side of the periodic table, and is particularly sensitive in the first row. There may be an application to biology because the density of (say) protein and water are not so very different leading to low contrast in the common mode.⁵⁶

B. Relation of Multiple Scattering Approach to HAADF

High Angular Aperture Dark Field (HAADF) as applied to tomography has been reviewed recently.⁵⁷ The principal advantages of HAADF in tomography are an insensitivity to Bragg scattering and its high Z dependence. The Bragg condition is

$$2d \sin \theta = n\lambda \quad (2)$$

where d is the lattice spacing, θ is the scattering angle, n is the order of the reflection, and λ is the wavelength of the incident radiation. For the case of a 300 keV electron, $\lambda = 1.969$ pm. A typical value for the spacing of low-index Bragg planes is (Si along (111) or $\sqrt{3}a/2$) 471 pm, so 2 mrad is a typical scattering angle for $n = 1$. By having the detector sensitive to scattering angles many times 2 mrad, the Bragg condition may be avoided in practice. In practice, a 40 mrad inner radius is typical.⁵⁷ Hence, the technique has had more application in material science (which often has crystalline samples) than in biology, where the assumption of an amorphous material is typically met.

To see the Z dependence in HAADF, consider the differential cross sections from the compilation of

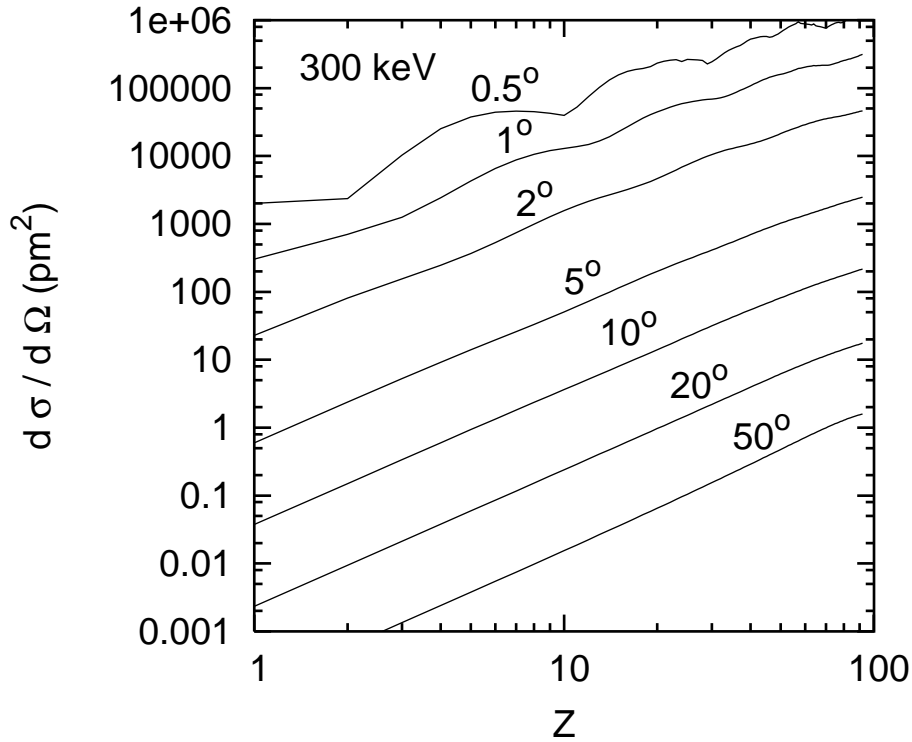


FIG. 8: Cross sections for the elements with atomic number Z from 1 to 92 for 300 keV electrons according to the calculations of Berger and Seltzer¹⁰ at the indicated scattering angles.

Berger and Seltzer¹⁰ for the angles shown in Fig. 8. Related plots were given earlier for 100 keV electrons.⁵⁸ For angles of 2° (35 mrad) or more, there is little influence from shell structure. Power law approximations to the curves of Fig. 8 are presented in Fig. 9. Taking the typical operating parameter for HAADF to be 40 mrad, a $Z^{1.68}$ dependence is obtained. A similar result was presented by Kirkland.⁵⁹ The present result may be compared to the dependence of the elastic cross section, shown in Fig. 10, which is approximately $Z^{1.45}$ with substantial modulation due to shell structure. In practice, HAADF is more sensitive to high Z elements than bright-field imaging by the ratio of these quantities, i.e., by $Z^{0.23}$. For a system composed of fairly widely varying atomic number such as gold ($Z = 79$) and carbon ($Z = 6$), the sensitivity of HAADF is seen to be a factor of about 1.9 more than bright-field imaging. However, since the signal in HAADF is typically 100 times less than in bright-field imaging, it is not so clear that even high Z elements will be better detected. This analysis suggests the principal advantage of HAADF is in avoiding the Bragg condition rather than increasing the sensitivity to high Z elements *per se*.

C. Mean Free Paths

Although cross sections are the traditional means of representing interaction strengths, it is more intuitive to consider the mean free paths, which are related to the cross section by $\tau = (n\sigma)^{-1}$ or $\tau^{(1)} = (n\sigma_1)^{-1}$ to the first transport coefficient σ_1 , where n is the number density. The number densities for most of the chemical elements are given in Fig. 11. The number density tends to peak in the middle of the rows of the periodic table; the relatively constant number density of the rare earth elements ($Z = 57$ to $Z = 71$) is also apparent. The number densities of Fig. 11 may be combined with the cross sections of Fig. 10 to yield τ and $\tau^{(1)}$ for the elements, shown in Fig. 12.

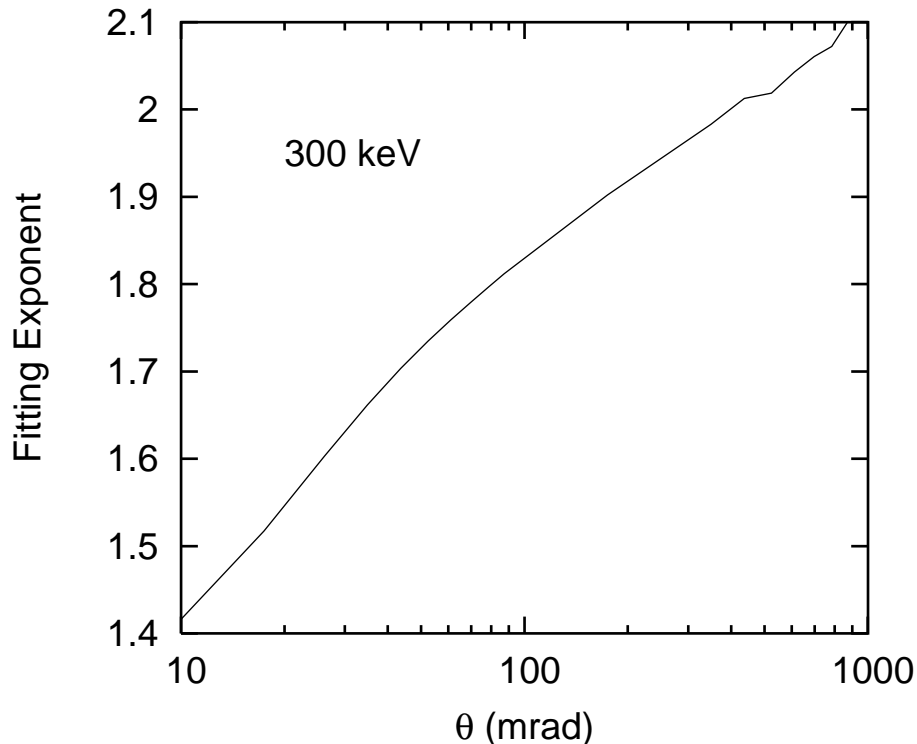


FIG. 9: Exponent of a power law fit to the data of Fig. 8. The atomic number Z is taken to the power of the fitting exponent. The Rutherford scattering result, expected to be valid at large angles, has the value of 2.

The theory developed in Ref. 48 requires the thickness of the sample to be small compared to $\tau^{(1)}$, i.e., typically small compared to $100 \mu\text{m}$ for low Z materials and small compared to $1 \mu\text{m}$ for the 5d transition metals. The electron beam ceases to have beam-like character after traversing a distance $\tau^{(1)}$ in the material. It is also notable that τ and $\tau^{(1)}$ come together somewhat for higher Z elements, which is related to the fact that the higher Z elements have larger differential cross sections at high angles. The theory does not impose a restriction that the sample not exceed the mean free path for elastic interactions τ , which is more or less the validity condition in the Beer's Law approach.

III. CONCLUSIONS

X-ray tomography and electron tomography have both advanced to the point where systems a few micrometers in size may be studied by either technique. Which probe is preferable will depend upon the desired resolution, the sample size, its chemical composition, state of crystallinity, and the available microscopes. The resolution in electron microscopes will degrade approximately as $Z^{1.45}$ for a fixed sample thickness and a little worse than the $t^{3/2}$ for a given material of thickness t . A recent theoretical advance in multiple scattering in electron tomography has yet to be exploited in experiments so the regime of few micrometer samples may open to electron tomography shortly.

X-ray microscopes based on Fresnel zone plates are limited to a resolution which is independent of Z . Taking 20 nm as the zone plate resolution, allowing a factor of 2 for the degradation from 2D to 3D images, electron microscopy should be competitive for low Z (e.g., biological) samples to thickness of about $3 \mu\text{m}$ based on the resolution of 8 nm achieved in a 1.2 nm thick sample.³⁹ Lensless x-ray microscopes

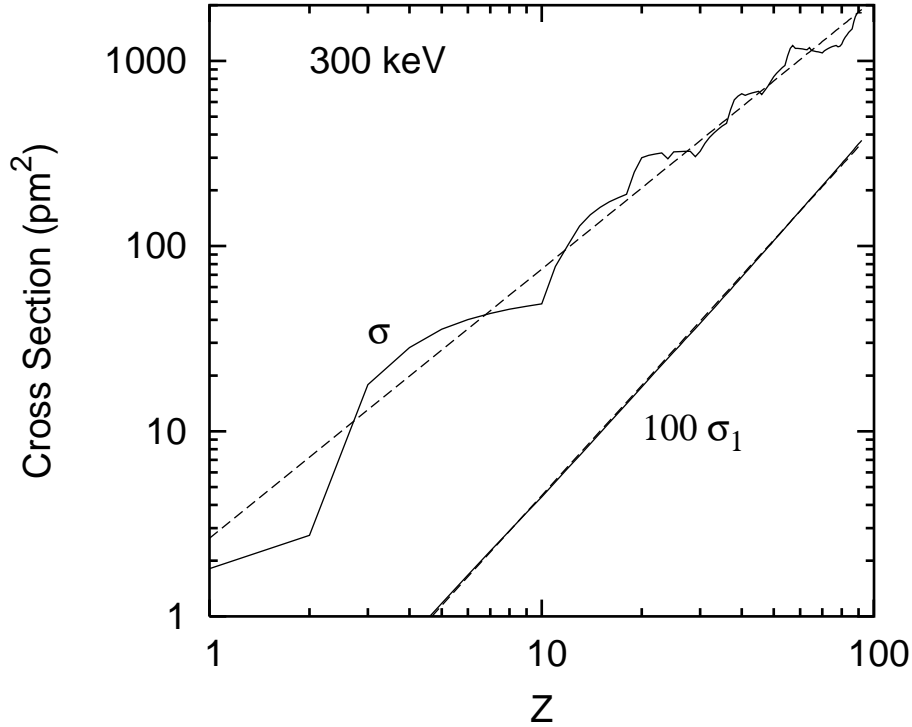


FIG. 10: Total cross section σ as a function of the atomic number Z and a fit $2.64Z^{1.454}$ pm^2 , as well as the first transport coefficient σ_1 which is fit by $0.000477Z^{1.975}$ pm^2 .

will be limited by the absorption in the material which showed strong edge dependence, however, these absorption coefficients vary approximately as the photon energy cubed⁶⁰ but the imaginary part of the dielectric constant varies only inversely with the energy¹⁴ it may be possible to use phase contrast with a wide range of materials. X-ray microscopes with and without zone-plate optics have also shown advances making their application to few micrometer samples more desirable. While x-ray techniques are in principle more broadly applicable than electron microscopy, in practice, electron microscopy will dominate where it can be applied. Both fields will be enriched by the possibility of intercomparison.

Acknowledgments

I wish to thank my many collaborators in microscopy and tomography over the past eight years, principally Uwe Arp, Sean Frigo, James Gao, Steven Grantham, Andrew Kalukin, Markus Kuhn, Theodore Levin, Thomas Lucatorto, Ian McNulty, Suneeta Neogi, I. Cev Noyan, David Paterson, Bruce Ravel, Cornelia Retsch, Wayne Roberge, John Henry Scott, Steven Seltzer, Eric Shirley, Charles Tarrío, I. C. Edmund Turcu, Steven Wang, and Nestor Zaluzec, as well as managers including Steven Kirch, Toh Ming Lu, Arye Shapiro, Anne Testoni, and David Vallett.

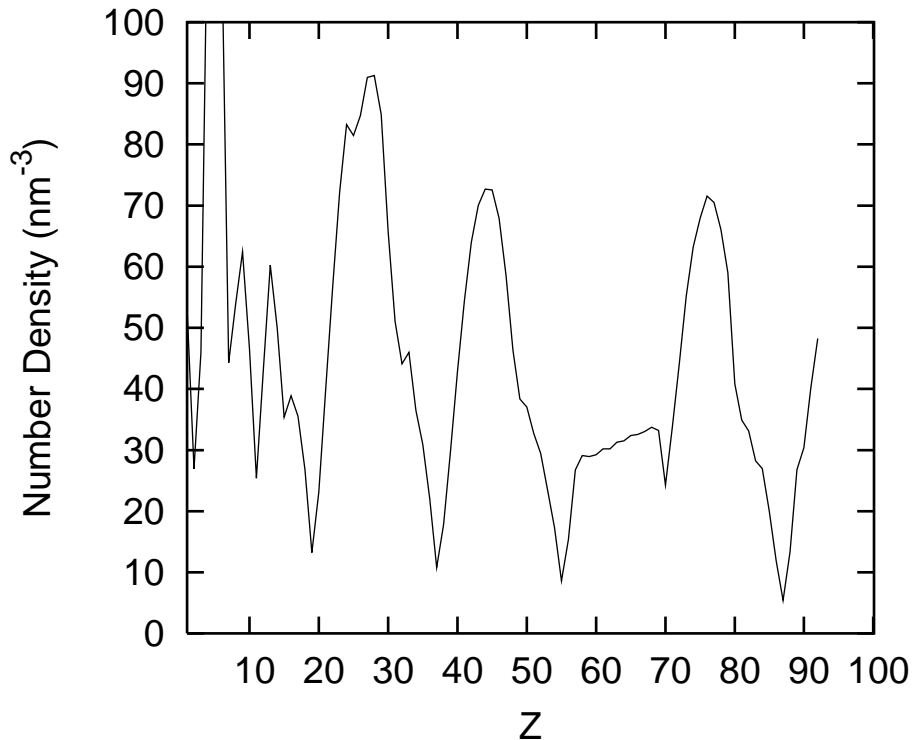


FIG. 11: The number densities of the chemical elements in their natural solid state.¹² The curve peaks at $Z = 5$ with 130 nm^{-3} .

-
- ¹ G. T. Herman, *Image reconstruction from projections: the fundamentals of computerized tomography* (Academic, New York, 1980).
- ² H. H. Barrett and W. Swindell, *Radiological Imaging* (Academic, New York, 1981), sec. 7.2.
- ³ A. C. Kak and M. Slaney, *Principles of computerized tomographic imaging* (IEEE Press, New York, 1988).
- ⁴ L. Grodzins, *Nucl. Inst. & Meth.* **206**, 541 (1983).
- ⁵ B. P. Flannery, H. W. Deckman, W. G. Roberge, and K. L. D'Amico, *Science* **237**, 1439 (1987).
- ⁶ W. B. Lindquist, S.-M. Lee, D. A. Coker, K. W. Jones, and P. Spanne, *Journal of Geophysical Research* **101**, 8297 (1996).
- ⁷ K. L. D'Amico, J. H. Dunsmuir, S. R. Furguson, B. P. Flannery, and H. W. Deckman, *Rev. Sci. Instr.* **63**, 574 (1992).
- ⁸ T. Takeda, Y. Itai, K. Hayashi, J. Nagata, and H. Yamaji, *Journal of Computer Assisted Tomography* **18**, 98 (1994).
- ⁹ G. Soum, A. Mousselli, F. Arnal, and P. Verdier, *Revue de Phys. Appl.* **22**, 1189 (1987).
- ¹⁰ M. J. Berger and S. M. Seltzer, *Database of Cross Sections for the Elastic Scattering of Electrons and Positrons by Atoms* (U.S. Dept. of Commerce, Gaithersburg, MD, 2000), NISTIR 6573, with CDROM.
- ¹¹ V. G. Molière, *Z. Naturforsch.* **3a**, 78 (1948).
- ¹² N. W. Ashcroft and N. D. Mermin, *Solid State Physics* (Holt, Rinehart and Winston, New York, 1976), pp. i-ii.
- ¹³ W. S. Haddad, I. McNulty, J. E. Trebes, E. H. Anderson, R. A. Levesque, and L. Yang, *Science* **266**, 1213 (1994).
- ¹⁴ J. Kirz, C. Jacobsen, and M. Howells, *Quarterly Reviews of Biophysics* **28**, 33 (1995).
- ¹⁵ J. Lehr, *Optik* **104**, 166 (1997).
- ¹⁶ Z. H. Levine, A. R. Kalukin, S. P. Frigo, I. McNulty, and M. Kuhn, *Appl. Phys. Lett.* **74**, 150 (1999).
- ¹⁷ Z. H. Levine, A. R. Kalukin, M. Kuhn, S. P. Frigo, I. McNulty, C. C. Retsch, Y. Wang, U. Arp, T. B. Lucatorto, B. D. Ravel, et al., *J. Appl. Phys.* **87**, 4483 (2000).

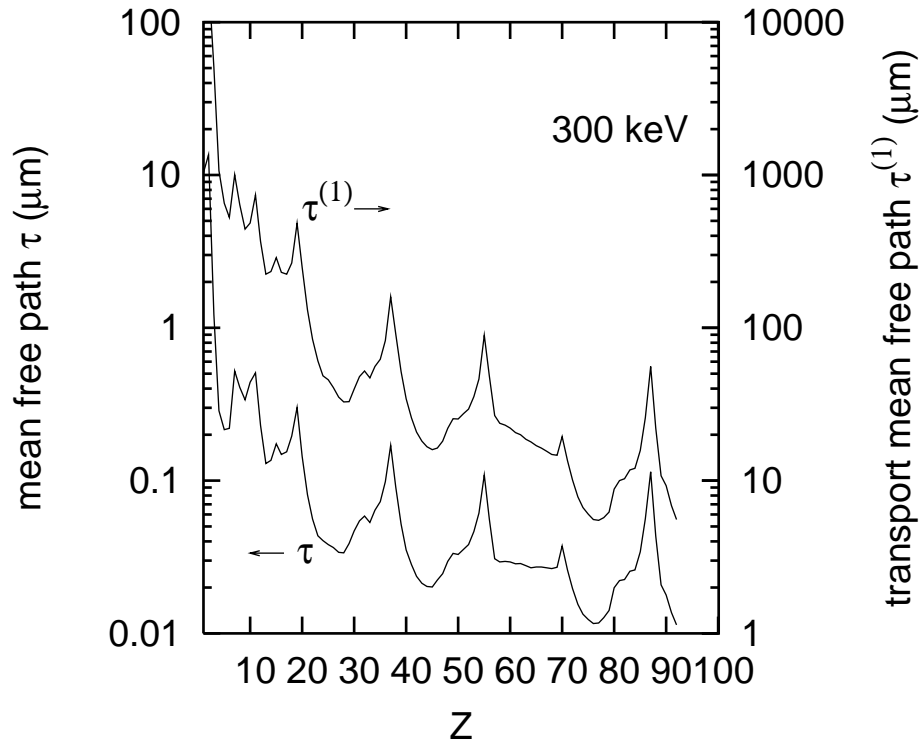


FIG. 12: The mean free path τ and transport mean free path $\tau^{(1)}$ for 300 keV electrons of the chemical elements based on the cross sections of Fig. 10 and the number densities of Fig. 11.

- ¹⁸ G. Schneider, E. Anderson, S. Vogt, C. Knochel, D. Weiss, M. Legros, and C. Larabell, *Surf. Rev. and Lett.* **9**, 177 (2002).
- ¹⁹ C. A. Larabell and M. A. L. Gros, *Molec. Bio. Cell* **15**, 957 (2004).
- ²⁰ W. Yun, S. Wang, D. Scott, and K. W. Nill, *Conf. Proc. 27th Int. Symp. for Testing and Failure Analysis* pp. 15–21 (2001), see also www.xradia.com. Certain commercial equipment, instruments, or materials are identified in this paper to foster understanding. Such identification does not imply recommendation or endorsement by NIST nor does it imply that the materials or equipment identified are necessarily the best available for the purpose.
- ²¹ A. G. Michette, *Optical systems for soft x-rays* (Plenum, New York, 1986).
- ²² E. Spiller, *Soft X-Ray Optics* (SPIE Optical Engineering Press, Bellingham, WA, 1994).
- ²³ E. H. Anderson, D. L. Olynick, B. Harteneck, E. Veklerov, G. Denbeaux, W. L. Chao, A. Lucero, L. Johnson, and D. Attwood, *J. Vac. Sci. & Tech. B* **18**, 2970 (2000).
- ²⁴ H. H. Solak, C. David, and J. Gobrecht, *Appl. Phys. Lett.* **85**, 2700 (2004).
- ²⁵ Institute of Physics, <http://optics.org/articles/news/10/12/6/1>.
- ²⁶ J. Miao, P. Charalambous, J. Kirz, and D. Sayre, *Nature* **400**, 342 (1999).
- ²⁷ J. W. Miao, T. Ishikawa, B. Johnson, E. H. A. nd B. Lai, and K. O. Hodgson, *Phys. Rev. Lett.* **89**, 088303 (2002).
- ²⁸ R. W. Gerchberg and W. O. Saxton, *Optik* **35**, 237 (1972).
- ²⁹ J. R. Fienup and A. M. Kowalczyk, *J. Opt. Soc. Am. A* **15**, 1662 (1998).
- ³⁰ V. Elser, *J. Opt. Soc. Am. A* **20**, 40 (2003).
- ³¹ J. Miao, D. Sayre, and H. N. Chapman, *J. Opt. Soc. Am. A* **15**, 1662 (1998).
- ³² K. A. Nugent, T. E. Gureyev, D. F. Cookson, D. Paganin, and Z. Barnea, *Phys. Rev. Lett.* **77**, 2961 (1996).
- ³³ T. E. Gureyev, *Opt. Comm.* **220**, 49 (2003).
- ³⁴ D. J. DeRosier and A. Klug, *Nature* **217**, 130 (1968).
- ³⁵ P. Gilbert, *J. Theor. Biol.* **36**, 105 (1972).
- ³⁶ J. R. McIntosh, *J. Cell Bio.* **153**, F25 (2001).
- ³⁷ B. F. McEwen and M. Marko, *J. Histochem. & Cytochem.* **49**, 553 (2001).

- ³⁸ B. Carragher and P. R. Smith, *J. Str. Biol.* **116**, 2 (1996).
- ³⁹ O. Medalia, I. Weber, A. S. Frangakis, D. Nicastro, G. Gerisch, and W. Baumeister, *Science* **298**, 1209 (2002).
- ⁴⁰ J. Mardinly, *Microscopy and Microanalysis* **7**, 510 (2001), suppl. 2: Proceedings.
- ⁴¹ R. Hegerl and W. Hoppe, *Z. Naturforsch.* **31a**, 1717 (1976).
- ⁴² B. F. McEwen, K. H. Downing, and R. M. Glaeser, *Ultramicroscopy* **60**, 357 (1995).
- ⁴³ K. R. Lata, P. A. Penczek, and J. Frank, *Ultramicroscopy* **58**, 381 (1995).
- ⁴⁴ J. Frank, J. Zhu, P. Penczek, Y. H. Li, S. Srivastava, A. Verschoor, M. Radermacher, R. Grassucci, R. K. Lata, and R. K. Agrawal, *Nature* **376**, 441 (1995).
- ⁴⁵ *J. S. Bio., J. Struct. Bio.* **116**, 71 (1996), see also <http://bio3d.colorado.edu/imod/>.
- ⁴⁶ Y. Liu, P. A. Penczek, B. F. McEwen, and J. Frank, *Ultramicroscopy* **58**, 393 (1995).
- ⁴⁷ Z. H. Levine, *Appl. Phys. Lett.* **82**, 3943 (2003).
- ⁴⁸ Z. H. Levine, *J. Appl. Phys.* **97**, 033101 (2005).
- ⁴⁹ S. P. Frigo, Z. H. Levine, and N. J. Zaluzec, *Appl. Phys. Lett.* **81**, 2112 (2002).
- ⁵⁰ Z. H. Levine, J. J. Gao, S. Neogi, T. M. Levin, J. H. Scott, and S. Grantham, *J. Appl. Phys.* **93**, 2193 (2003).
- ⁵¹ L. Reimer, *Transmission electron microscopy: physics of image formation and microanalysis, fourth ed.* (Springer, Berlin, 1997).
- ⁵² S. Goudsmit and J. L. Saunderson, *Phys. Rev.* **57**, 24 (1940).
- ⁵³ L. Reimer, *Transmission electron microscopy: physics of image formation and microanalysis, fourth ed.* (Springer, Berlin, 1997), sec. 5.4.3.
- ⁵⁴ J. D. Jackson, *Classical Electrodynamics, second ed.* (Wiley, New York, 1975), sect. 13.8, esp. Eq. (13.111).
- ⁵⁵ S. Goudsmit and J. L. Saunderson, *Phys. Rev.* **58**, 36 (1940).
- ⁵⁶ Z. H. Levine and M. Varner, unpublished.
- ⁵⁷ P. A. Midgeley and M. Weyland, *Ultramicroscopy* **96**, 413 (2003).
- ⁵⁸ E. J. Kirkland, R. F. Loane, and J. Silcox, *Ultramicroscopy* **23**, 77 (1987).
- ⁵⁹ E. J. Kirkland, *Advanced Computing in Electron Microscopy* (Plenum, New York, 1998), p. 93.
- ⁶⁰ A. H. Compton and S. K. Allison, *X-Rays in Theory and Experiment, second ed.* (Van Nostrand, Princeton, 1935), sect. VII.6-8.